UC Berkeley
UC Berkeley Previously Published Works

Title

Characteristics of plasma plume in ultrafast laser ablation with a weakly ionized air channel.

Permalink

Journal

ISSN

Authors

Hou, Huaming
Yang, Bo
Mao, Xianglei
et al.

Publication Date

DOI

Peer reviewed

Characteristics of plasma plume in ultrafast laser ablation with a weakly ionized air channel

HUAMING HOU,[1,2] BO YANG,[3,4] XIANGLEI MAO,[2,*] VASSILIA ZORBA,[2] PENGXU RAN,[5] AND RICHARD E. RUSSO[2]

[1]Key Laboratory of Advanced Technologies of Materials, Ministry of Education, Southwest Jiaotong University, Chengdu, Sichuan 610031, China
[2]Lawrence Berkeley National Laboratory, Berkeley, CA 94720, USA
[3]Department of Mechanical and Aerospace Engineering, University of Texas, Arlington, TX 76019, USA
[4]Corning Incorporated, Corning, New York 14831, USA
[5]The Peac Institute of Multiscale Sciences, Chengdu, Sichuan 610031, China
*x_mao@lbl.gov

Abstract: We report the influence of femtosecond (fs) laser weakly ionized air channel on characteristics of plasma induced from fs-laser ablation of solid Zr metal target. A novel method to create high temperature, low electron density plasma with intense elemental emission and weak bremsstrahlung emission was demonstrated. Weakly ionized air channel was generated as a result of a non-linear phenomenon. Two-dimensional time-resolved optical-emission images of plasma plumes were taken for plume dynamics analysis. Dynamic physical properties of filament channels were simulated. In particular, we investigated the influence of weakly ionized air channel on the evolution of solid plasma plume. Plasma plume splitting was observed whilst longer weakly ionized air channel formed above the ablation spot. The domination mechanism for splitting is attributed to the long-lived underdense channel created by fs-laser induced weakly ionization of air. The evolutions of atomic/molecular emission intensity, peak broadening, and plasma temperature were analyzed, and the results show that the part of plasma entering weakly ionized air channel features higher initial temperature, lower electron density and faster decay.

References and links

1. M. Kretschmar, C. Brée, T. Nagy, A. Demircan, H. G. Kurz, U. Morgner, and M. Kovačev, "Direct observation of pulse dynamics and self-compression along a femtosecond filament," Opt. Express **22**(19), 22905–22916 (2014).
2. S. Kanehira, J. Si, J. Qiu, K. Fujita, and K. Hirao, "Periodic nanovoid structures via femtosecond laser irradiation," Nano Lett. **5**(8), 1591–1595 (2005).
3. O. Lahav, L. Levi, I. Orr, R. Nemirovsky, J. Nemirovsky, I. Kaminer, M. Segev, and O. Cohen, "Long-lived waveguides and sound-wave generation by laser filamentation," Phys. Rev. A **90**(2), 021801 (2014).
4. E. J. Judge, G. Heck, E. B. Cerkez, and R. J. Levis, "Discrimination of composite graphite samples using remote filament-induced breakdown spectroscopy," Anal. Chem. **81**(7), 2658–2663 (2009).
5. W. Liu and S. Chin, "Direct measurement of the critical power of femtosecond Ti:sapphire laser pulse in air," Opt. Express **13**(15), 5750–5755 (2005).
6. S. L. Chin, T.-J. Wang, C. Marceau, J. Wu, J. S. Liu, O. Kosareva, N. Panov, Y. P. Chen, J.-F. Daigle, S. Yuan, A. Azarm, W. W. Liu, T. Seideman, H. P. Zeng, M. Richardson, R. Li, and Z. Z. Xu, "Advances in intense femtosecond laser filamentation in air," Laser Phys. **22**(1), 1–53 (2012).
7. M. Rodriguez, R. Bourayou, G. Méjean, J. Kasparian, J. Yu, E. Salmon, A. Scholz, B. Stecklum, J. Eislöffel, U. Laux, A. P. Hatzes, R. Sauerbrey, L. Wöste, and J. P. Wolf, "Kilometer-range nonlinear propagation of femtosecond laser pulses," Phys. Rev. E - Stat. Nonlinear, Soft Matter Phys. **69**, 1–7 (2004).
8. M. Durand, A. Houard, B. Prade, A. Mysyrowicz, A. Durécu, B. Moreau, D. Fleury, O. Vasseur, H. Borchert, K. Diener, R. Schmitt, F. Théberge, M. Chateauneuf, J.-F. Daigle, and J. Dubois, "Kilometer range filamentation," Opt. Express **21**(22), 26836–26845 (2013).

9. F. Théberge, W. Liu, P. T. Simard, A. Becker, and S. L. Chin, "Plasma density inside a femtosecond laser filament in air: Strong dependence on external focusing," Phys. Rev. E Stat. Nonlin. Soft Matter Phys. **74**(3), 036406 (2006).
10. Q. Sun, H. Asahi, Y. Nishijima, N. Murazawa, K. Ueno, and H. Misawa, "Pulse duration dependent nonlinear propagation of a focused femtosecond laser pulse in fused silica," Opt. Express **18**(24), 24495–24503 (2010).
11. Y. H. Chen, S. Varma, T. M. Antonsen, and H. M. Milchberg, "Direct measurement of the electron density of extended femtosecond laser pulse-induced filaments," Phys. Rev. Lett. **105**(21), 215005 (2010).
12. X. Sun, S. Xu, J. Zhao, W. Liu, Y. Cheng, Z. Xu, S. L. Chin, and G. Mu, "Impressive laser intensity increase at the trailing stage of femtosecond laser filamentation in air," Opt. Express **20**(4), 4790–4795 (2012).
13. S. Xu, X. Sun, B. Zeng, W. Chu, J. Zhao, W. Liu, Y. Cheng, Z. Xu, and S. L. Chin, "Simple method of measuring laser peak intensity inside femtosecond laser filament in air," Opt. Express **20**(1), 299–307 (2012).
14. H. L. L. Xu, G. Méjean, W. Liu, Y. Kamali, J.-F. F. Daigle, A. Azarm, P. T. T. Simard, P. Mathieu, G. Roy, J.-R. R. Simard, and S. L. L. Chin, "Remote detection of similar biological materials using femtosecond filament-induced breakdown spectroscopy," Appl. Phys. B **87**(1), 151–156 (2007).
15. P. Rohwetter, K. Stelmaszczyk, L. Wöste, R. Ackermann, G. Méjean, E. Salmon, J. Kasparian, J. Yu, and J.-P. Wolf, "Filament-induced remote surface ablation for long range laser-induced breakdown spectroscopy operation," Spectrochim. Acta Part B At. Spectrosc. **60**, 1025–1033 (2005).
16. K. Stelmaszczyk, P. Rohwetter, G. Méjean, J. Yu, E. Salmon, J. Kasparian, R. Ackermann, J.-P. Wolf, and L. Wöste, "Long-distance remote laser-induced breakdown spectroscopy using filamentation in air," Appl. Phys. Lett. **85**(18), 3977–3979 (2004).
17. D. Mirell, O. Chalus, K. Peterson, and J.-C. Diels, "Remote sensing of explosives using infrared and ultraviolet filaments," J. Opt. Soc. Am. B **25**(7), B108–B111 (2008).
18. I. Ghebregziabher, K. C. Hartig, and I. Jovanovic, "Propagation distance-resolved characteristics of filament-induced copper plasma," Opt. Express **24**(5), 5263–5276 (2016).
19. H. Hou, G. C.-Y. Chan, X. Mao, R. Zheng, V. Zorba, and R. E. Russo, "Femtosecond filament-laser ablation molecular isotopic spectrometry," Spectrochim. Acta Part B At. Spectrosc. **113**, 113–118 (2015).
20. S. Zahedpour, J. K. Wahlstrand, and H. M. Milchberg, "Quantum Control of Molecular Gas Hydrodynamics," Phys. Rev. Lett. **112**(14), 143601 (2014).
21. N. Jhajj, E. W. Rosenthal, R. Birnbaum, J. K. Wahlstrand, and H. M. Milchberg, "Demonstration of Long-Lived High-Power Optical Waveguides in Air," Phys. Rev. X **4**(1), 011027 (2014).
22. G. Point, C. Milián, A. Couairon, A. Mysyrowicz, and A. Houard, "Generation of long-lived underdense channels using femtosecond filamentation in air," J. Phys. At. Mol. Opt. Phys. **48**(9), 094009 (2015).
23. A. Ryabtsev, S. Pouya, M. Koochesfahani, and M. Dantus, "Vortices in the wake of a femtosecond laser filament," Opt. Express **22**(21), 26098–26102 (2014).
24. O. Graydon, "Filament vortices," Nat. Photonics **8**(12), 886 (2014).
25. S. S. Harilal, P. K. Diwakar, M. P. Polek, and M. C. Phillips, "Morphological changes in ultrafast laser ablation plumes with varying spot size," Opt. Express **23**(12), 15608–15615 (2015).
26. K. Oguri, Y. Okano, T. Nishikawa, and H. Nakano, "Dynamics of femtosecond laser ablation studied with time-resolved x-ray absorption fine structure imaging," Phys. Rev. B **79**(14), 144106 (2009).
27. S. S. Harilal, N. Farid, J. R. Freeman, P. K. Diwakar, N. L. LaHaye, and A. Hassanein, "Background gas collisional effects on expanding fs and ns laser ablation plumes," Appl. Phys. A Mater. Sci. Process. **117**, 1–8 (2014).
28. H. Zhang, F. Zhang, X. Du, G. Dong, and J. Qiu, "Influence of laser-induced air breakdown on femtosecond laser ablation of aluminum," Opt. Express **23**(2), 1370–1376 (2015).
29. E. W. Rosenthal, J. P. Palastro, N. Jhajj, S. Zahedpour, J. K. Wahlstrand, and H. M. Milchberg, "Sensitivity of propagation and energy deposition in femtosecond filamentation to the nonlinear refractive index," J. Phys. At. Mol. Opt. Phys. **48**(9), 094011 (2015).
30. J. Siegel, G. Epurescu, A. Perea, F. J. Gordillo-Vázquez, J. Gonzalo, and C. N. Afonso, "High spatial resolution in laser-induced breakdown spectroscopy of expanding plasmas," Spectrochim. Acta - Part B At. Spectrosc. **60**, 915–919 (2005).
31. J. F. Daigle, A. Jaroń-Becker, S. Hosseini, T. J. Wang, Y. Kamali, G. Roy, A. Becker, and S. L. Chin, "Intensity clamping measurement of laser filaments in air at 400 and 800 nm," Phys. Rev. A – At. Mol. Opt. Phys. **82**, 1–5 (2010).
32. H. L. Xu, A. Azarm, J. Bernhardt, Y. Kamali, and S. L. Chin, "The mechanism of nitrogen fluorescence inside a femtosecond laser filament in air," Chem. Phys. **360**(1-3), 171–175 (2009).
33. A. Lofthus and P. Krupenie, "The spectrum of molecular nitrogen," Phys. Chem. Ref. Data **6**(1), 113–307 (1977).
34. A. Talebpour, J. Yang, and S. L. Chin, "Semi-empirical model for the rate of tunnel ionization of N2 and O2 molecule in an intense Ti:sapphire laser pulse," Opt. Commun. **163**(1-3), 29–32 (1999).
35. S. L. Chin, S. A. Hosseini, W. Liu, Q. Luo, F. Théberge, N. Aközbek, A. Becker, V. P. Kandidov, O. G. Kosareva, and H. Schroeder, "The propagation of powerful femtosecond laser pulses in opticalmedia: physics, applications, and new challenges," Can. J. Phys. **83**(9), 863–905 (2005).
36. A. Talebpour and M. Abdel-Fattah, "Spectroscopy of the gases interacting with intense femtosecond laser pulses," Laser Phys. **11**, 68–76 (2001).

37. Q. Luo, S. Hosseini, B. Ferland, and S. L. Chin, "Backward time-resolved spectroscopy from filament induced by ultrafast intense laser pulses," Opt. Commun. **233**(4-6), 411–416 (2004).
38. G. Gariepy, N. Krstajić, R. Henderson, C. Li, R. R. Thomson, G. S. Buller, B. Heshmat, R. Raskar, J. Leach, and D. Faccio, "Single-photon sensitive light-in-fight imaging," Nat. Commun. **6**(1), 6021 (2015).
39. H. Hou, G. C.-Y. Chan, X. Mao, V. Zorba, R. Zheng, and R. E. Russo, "Femtosecond laser ablation molecular isotopic spectrometry for zirconium isotope analysis," Anal. Chem. **87**(9), 4788–4796 (2015).
40. E. F. Toro, *Riemann Solvers and Numerical Methods for Fluid Dynamics* (Springer Berlin Heidelberg, 2009).
41. Y. H. Cheng, J. K. Wahlstrand, N. Jhajj, and H. M. Milchberg, "The effect of long timescale gas dynamics on femtosecond filamentation," Opt. Express **21**(4), 4740–4751 (2013).
42. S. Tzortzakis, B. Prade, M. Franco, A. Mysyrowicz, S. Hüller, and P. Mora, "Femtosecond laser-guided electric discharge in air," Phys. Rev. E Stat. Nonlin. Soft Matter Phys. **64**(5), 057401 (2001).
43. J. K. Wahlstrand, N. Jhajj, E. W. Rosenthal, S. Zahedpour, and H. M. Milchberg, "Direct imaging of the acoustic waves generated by femtosecond filaments in air," Opt. Lett. **39**(5), 1290–1293 (2014).
44. F. Lowater, "The band spectrum of zirconium oxide," Proc. Phys. Soc. **44**(1), 51–66 (1932).
45. S. P. Davis and P. D. Hammer, "Energy levels of zirconium oxide," Astrophys. J. **332**, 1090–1091 (1988).
46. K. K. Anoop, X. Ni, M. Bianco, D. Paparo, X. Wang, R. Bruzzese, and S. Amoruso, "Two-dimensional imaging of atomic and nanoparticle components in copper plasma plume produced by ultrafast laser ablation," Appl. Phys., A Mater. Sci. Process. **117**, 1–6 (2014).
47. S. S. Harilal, B. E. Brumfield, B. D. Cannon, and M. C. Phillips, "Shock Wave Mediated Plume Chemistry for Molecular Formation in Laser Ablation Plasmas," Anal. Chem. **88**(4), 2296–2302 (2016).
48. D. W. Hahn and N. Omenetto, "Laser-induced breakdown spectroscopy (LIBS), part I: review of basic diagnostics and plasma-particle interactions: still-challenging issues within the analytical plasma community," Appl. Spectrosc. **64**(12), 335–366 (2010).
49. G. C.-Y. Chan, I. Choi, X. Mao, V. Zorba, O. P. Lam, D. K. Shuh, and R. E. Russo, "Isotopic determination of uranium in soil by laser induced breakdown spectroscopy," Spectrochim. Acta Part B At. Spectrosc. **122**, 31–39 (2016).

1. Introduction

The propagation of ultrafast laser filaments through transparent media contains complex nonlinear phenomena and results in various exciting potential applications [1–4]. A filament can be formed when femtosecond (fs) laser power is above the critical power [5], as a result of dynamic balance between self-focusing and defocusing [6]. The length of filament varies from several times of Rayleigh length to kilometer range [7,8], which is focus conditions and laser parameters dependent [9,10]. The typical diameter of filament is around 100 μm [11]. The laser power density clamped in the filament channels is in the order of 10^{13} W/cm^2 or even higher [12,13], which is sufficient for material ablation. Fs-laser filament ablation, as a unique material processing and analysis technique, provides distinct advantages over nanosecond laser ablation. Remote chemical analysis with fs-laser filament ablation has been demonstrated [4,14–17].

The fs-laser intensity clamped inside the filament core is propagation distance dependence, and the characteristics of filament induced plasma over propagation distance are significantly different [18]. Due to the non-linear effect during fs-laser propagation, air molecules can be weakly ionized and a weakly ionized air channel forms. The interaction between fs-laser induced solid plasma and fs-laser induced weakly ionized air channel was seldom reported. Understanding the role of preexistent weakly ionized air channel in evolution of fs-laser induced solid plasma from sample is important for improving the performance of remote-filament induced breakdown spectroscopy (R-FIBS) or femtosecond filament-laser ablation molecular isotopic spectrometry (F^2-LAMIS) [19]. The self-focused fs-laser beam can heat up the gas [20], generate shockwave [3,21], modify local air density [21,22], and create vortex [23,24]. The plasma dynamics differs from that generated in quasi-static ambient or pressure reduced environment [25–27]. More complex mechanism is included in case of fs-laser filament ablation of materials, compared to typical fs-laser ablation cases because a weakly ionized air channel was created before solid plasma expansion [28]. Understanding the plasma plume dynamics of a fs-laser induced plasma in weakly ionized air channel is ultimately important for many applications. In case of fs-laser filament ablation of materials, the plasma evolution can be affected by the weakly ionized

channel [29]. The dynamics and density gradient [22] of air molecules resulted from weakly ionized air channel set a special environment that plasma expands inside.

In this letter, a threadlike weakly ionized air channel was created by pre-focusing fs-laser beams with lens. The laser energy was clamped inside the channel and then was coupled onto sample surface. Plasma was induced on solid sample surface. We report the characteristics of the ablated plasma plume from solid zirconium metal target. Zr metal target was placed at different locations of the air channels. The dynamics of fs-laser ablated plasma plume was analyzed by recording time-resolved optical-emission images of plasma plumes. The dynamics of the weakly ionized air channel were simulated and its influence on the evolution of plasma was investigated.

2. Experimental setup

The laser source was a Ti:Sapphire fs-laser system (λ = 800 nm, 35 fs pulse, Coherent, Astrella). Constant laser energy of 5 mJ was used. By focusing laser beam with a f = 15 cm lens, a weakly ionized air channel was generated above the geometrical focus. Fluoresce emission of the ionized channel was directly imaged onto the entrance slit of a spectrograph (Horiba 1250M) by a pair of lenses. Laser beam propagation direction lied along the orientation of the spectrograph slit. To record spectra with high spectral resolution (~10 pm), 3600 g/mm grating was used. An intensified-CCD (PI-MAX, 1340 x 1300 pixels, 20 x 20 μm^2 pixel size) was positioned at the spectrograph exit plane. Time resolved images of plasma/weak ionized channel were recorded with configuration of spectrograph grating operating in reflection mode with fully opened entrance slit (3 mm) [30]. Alternatively, the spectrograph produced 1D-spatial and spectral images of the ionized channel or ablated plasmas, with configuration of spectrograph grating operating in diffraction mode with narrow slit width (e.g., 50 μm). The ICCD gate was synchronized with laser pulse and the time zero coincided with the irradiation of the laser pulse. The imaging magnification was 3.3 × . Flatfield calibration was done for all spectra. For plasma plume images and emission spectra measurements, a zirconium plate sample was used. The sample was mounted on a three dimensional stage. Measurements were carried out in ambient air (Fig. 1).
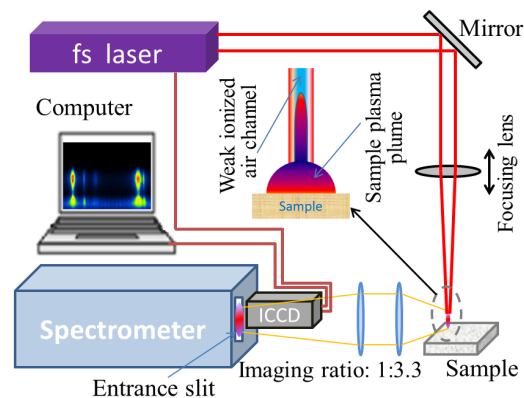

Fig. 1. Experimental setup.

3. Results and discussion

3.1 Weakly ionized air channel

Filament can form in air whilst the power of the fs-laser pulses is above the critical power (P_{cr}) for self-focusing. If the laser pulse peak power is lower than the critical power, filamentation cannot be launched [10]. In this experiment, the laser power is about one order higher than P_{cr} that reported for fs-laser pulses at 800 nm in air [5]. The observed length of N_2^+ emission zone is >3 times as long as the Rayleigh length (~1.4 mm), and the emission is

very similar to the fluorescence emitted from filaments launched by focusing fs-laser beam with f = 11-100 cm lens [13,31,32]. Figure 2(a) shows the emission image of the weakly ionized air channel. A 10 nm bandpass filter centered at 390 nm was used, which only allowed the emission of ($\Delta \upsilon = 0$) band of first negative system of N_2^+ with bandhead at 391 nm [13,33] can be effectively imaged. The continuum spectral component contributed to the image is ignorable because fs-laser induced multiphoton or tunnel ionization [34,35] of air lead to clean fluorescence (i.e., almost free from plasma continuum) emitted from nitrogen molecule (N_2) and ion (N_2^+) [31,36,37], which was also confirmed in our experiment, as shown in Fig. 2(b). As seen in Fig. 2(a), the weakly ionized air channel forms at distances shorter than the geometrical focus of the lens, which was determined with following steps: 1) attenuating laser power to ablation threshold of silicon, 2) a polished silicon wafer was placed at different positions near the focus, 3) position with smallest crater size was set as the geometrical focus. The laser beam can pass through the fluorescing zone [38]. Only one single channel formed, which enhanced the interaction between weakly ionized channel and ablated plasma plume because higher laser intensity can be clamped inside the channel, thus intense influence of weakly ionized air channel on plasma plumes was expected. Moreover, the rotational temperature was calculated by fitting the experimental spectrum with synthetic first negative system of N_2^+ ($B^2\Sigma_u^+ \rightarrow X^2\Sigma_g^+$) molecular band, and the calculation yield an initial temperature of ~1200 K. Detailed simulation algorithm and fitting method can be found in our previously reports [19,39].
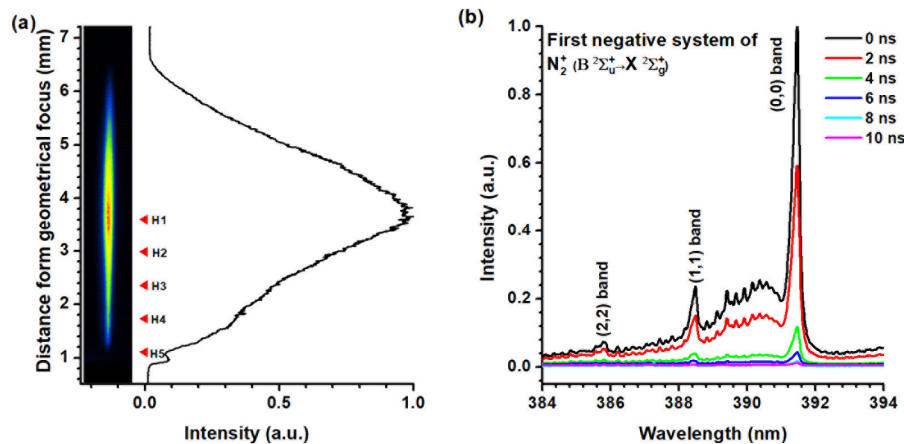

Fig. 2. (a): Air filament fluorescence image and longitudinal intensity distribution. Red triangles indicate the sample surface positions for following experiments. 1000 laser pulses were accumulated and the ICCD gate delay and gate width were 0 and 10 ns, respectively. The persistent time of fluorescence is less than 10 ns, which was experimentally confirmed, as shown in (b). The spectra shown in (b) were taken with 2 ns gate width.

3.2 Simulation of dynamic physical properties of filament channels

It is assumed that the hydrodynamic motion and thermal conduction of the gas are the dominant processes occurring at time scales of tens of nanosecond and longer, which are much greater than those of the fs-laser-gas interactions including photoionization and thermalization. The energy deposition profile is assumed to be spatially confined to the region of the initial photoionization events. Furthermore, on the nanosecond time scales the gas is assumed to be fully recombined and in local thermodynamic equilibrium. The axis symmetry is assumed for the problem along the longitudinal axis of the tube. The effect of longitudinal variation is neglected, hence effectively reducing the problem to one-dimension. Initially, it sets a uniform gas density, pressure, temperature and zero velocity field. At the beginning of simulation, a high temperature field (and hence a high pressure field) is imposed over the

center area with a Gaussian profile. The peak temperature is 1200 K, with a radial half width of 30 μm. The gas is then let evolve according to the following equations.

The conservation laws of mass, (linear) momentum, and energy require

$$\frac{\partial n}{\partial t} + \nabla \cdot j_n = 0, \tag{1}$$

$$\frac{\partial (np)}{\partial t} + \nabla \cdot (j_n p) = \nabla \cdot \sigma, \tag{2}$$

$$\frac{\partial (n\varepsilon)}{\partial t} + \nabla \cdot (j_n \varepsilon) = \nabla \cdot j_k + \nabla \cdot (\sigma \cdot v), \tag{3}$$

where n is the number density of gas molecules, v is the hydrodynamic velocity, $p (\equiv mv)$ and ε are the (average) momentum and energy per molecule, respectively, m is the molecular mass, σ is the stress tensor, j_n is the mass flux, j_k is the partial energy flux due to energy/heat conduction, and t is the time. The constitutive laws for the fluxes and stress are given by

$$j_n = nv, \tag{4}$$

$$\sigma = -(P + \lambda \nabla \cdot v) I + \eta (\nabla v + \nabla^T v), \tag{5}$$

$$j_k = k \nabla \varepsilon, \tag{6}$$

where k is the energy conduction coefficient, η and λ are the first and second coefficients of viscosity, P is the thermodynamic pressure, I is the identity matrix, and the superscript T denotes the transpose of a matrix. For simplicity, it is set that $\lambda = 2\eta / 3$. For an ideal gas, $P = nk_B T$, where T is the temperature. The total energy is partitioned into thermal and kinetic energy as $\varepsilon \equiv C_V T + \frac{m}{2} v \cdot v$, where C_V is the specific heat capacity at fixed volume, v is the velocity of molecules. k / C_V is the thermal conductivity, denoted by κ. For the case of atmospheric air, we assume a single-component gas with initial number density n = 2.5 × 10^{25} molecules/m³ and average mass m = 29 g/mol. The viscosity and thermal diffusivity are given by $\eta = \eta_0 \sqrt{T / T_0}$ and $\kappa = \kappa_0 \sqrt{T / T_0}$, with η_0 = 1.81 × 10^{-5} Pa-s, κ_0 = 0.024 W/m-K, and T_0 = 293 K. Specific heat C_V = 20.8 J/mol-K.
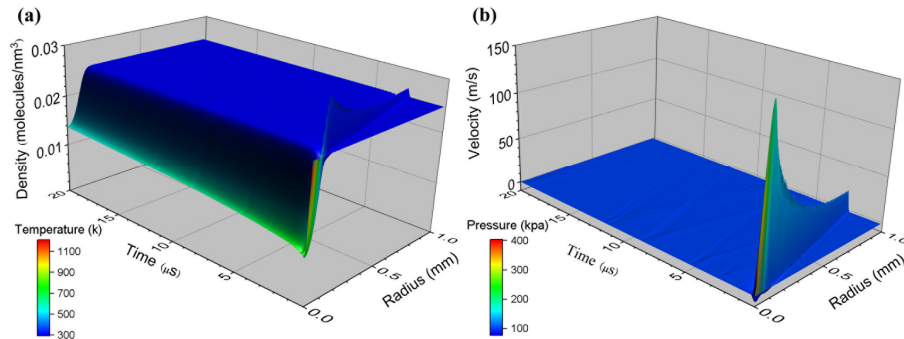

Fig. 3. The time evolution of (a) density and (b) radical velocity component v_r as color-coded by temperature in K and the radical pressure component (-σ_r) in kPa, respectively.

The above initial-boundary value problem is solved numerically by applying a standard finite volume method [40]. The domain is discretized in a rectangular mesh of finite volumes. The nodes are assigned to the centers of the finite volumes. The fluxes of mass, momentum and energy at the boundaries of the finite volumes are evaluated by finite difference approximations based on nodal values of density, velocity, and energy (temperature). The conservation laws are enforced with these fluxes in a local integral form. By the finite volume method, the conservation laws are ensured between finite volumes, even though the time derivatives and the fluxes are approximate. The time derivative is approximated by first-order finite difference, whilst the spatial derivative by the third-order finite difference. The time step is 1 ns.

The time resolved density, temperature, radical temperature and radial velocity of the weakly ionized air channel were shown in Fig. 3. The weakly ionized air channel induced from fs-laser filamentation only persists for about 10 ns and repartitions its energy into the translational and rotational degrees of freedom of air molecules [41]. An outward-propagating pressure wave formed after the localized, fast energy deposition, after that a low density channel was created, which featured similar cylindrical geometry as filament channels [42,43]. The density reduction can be up to 70%, and lasts for over hundreds of microseconds. A long-lived underdense channel or density cylindered hole is left behind fs-laser filament, and it persists enough time to modify the filament induced plasma plumes.

3.3 Expansion of fs-laser ablated plasma plume in weakly ionized air channel

In order to investigate the influence of the weakly ionized air channel on fs-laser plasma plumes, a zirconium sample was positioned at locations H1-H5, as indicated in Fig. 2(a). The spatiotemporal evolution of plume was recorded. Zirconium is line rich element and molecular band spectra of ZrO are also rich in laser induced plasma emission, as demonstrated in our previous report [39]. A 10 nm bandpass filter centered at 460 nm was used whilst recording the images of plasma plume. Tens of Zr atomic/ionic lines and three $\alpha(0,0)$ ZrO molecular bands of $d^3\Delta$–$a^3\Delta$ system [44,45] were covered in transmission wavelength range of the filter. The time resolved images of fs-laser induced plasmas from zirconium metal sample that positioned at five different positions (H1 to H5) are shown in Fig. 4. The intensity of each image was scaled to 0-1 to ensure that each image features high contrast. Under the irradiation effect of fs-laser, plasma formed at the surface of sample. For the plasmas generated at location H1, the radial and longitudinal expansion velocities were similar at early stage time delays (0 to 100 ns) and plasmas were spherical. When the time delay was over 150 ns, the height of plasma kept increasing whilst the radical size was nearly constant, until the final plasma decay around 4 μs. The plasmas were not symmetric in the longitudinal direction, but feature a hot spot in the part near sample surface (~1 mm) and a weak tail propagating upward. Although no obviously difference was observed at early stage (0 to 50 ns) plasmas induced from samples positioned at locations of H1 to H5, several distinguish differences were observed by comparing the sequence images. Obvious plasma splitting was observed when the sample was positioned at locations H3, H4 and H5, a dark area presented between the two separated parts and the height of this area was larger whereas the sample was positioned closer to the geometrical focus. The relative intensity of the two separated parts differentiated. The shorter distance between sample surface and geometrical focus, the splitting time occurred earlier, but the plasma portion at the top decayed faster.

Triple splitting structure of plasma plume has been reported with fs-laser ablation of metal targets in vacuum condition, and the corresponding mechanism was attributed to that the ions, neutrals, and nanoparticles propagated with decreasing velocity [25,46]. However, in this work, we did not observe significant difference between distributions of atomic and ionic species in two split plumes by spectroscopic analysis of plasma plume emission (see section 3.3), we rule out that propagating velocity difference that leads to plume splitting. Moreover, we did not observe plume splitting whilst sample surface was positioned at location H1.

Harilal *et al* [25] reported the morphological changes in fs-laser ablated plumes with varying spot sizes, and no plume splitting phenomenon was observed, even though the angular distributions of ejected plasma varies greatly with spot sizes and the shape of plumes changes from spherical to cylindrical with an increasing spot size from 100 to 600 μm. The weakly ionized air channel generated a specific environment for the expansion of plasma plume. The underdense feature of the channel is likely the dominate mechanism for the splitting and the channel persists enough time to modify the filament induced plasma plumes. Due to the density gradient between plasma plume and filament induced underdense channel, part of the plasma plume can be sucked into the low density channels, as shown in Fig. 3(H2)-3(H5).
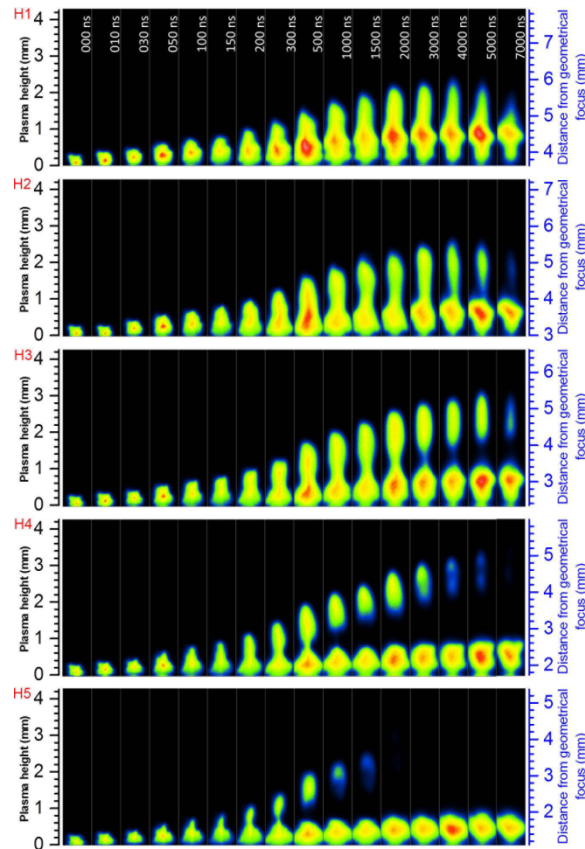

Fig. 4. Time resolved images of fs-laser induced plasmas from zirconium metal sample positioned at five different locations as indicated in Fig. 1.

3.4 Spectroscopic analysis

In order to characterize the two split plasma plumes, spectroscopic analysis was performed. The plasmas induced at location H4 was analyzed because optical emissions of both two split plasma plumes persisted longer and the distance between two plumes was larger, compared to that of other locations, as shown in Fig. 4. Figure 5 shows the temporal and spatial resolved plasma emission spectra recorded by two dimensional ICCD array. Intensity was scaled to 0-1 for each sub frame. The spectra shown in Fig. 5 cover from 461.84 to 463.74 nm. At early time, intense continuum emission contributes to the main component of measured spectrum. At delay time of 500 ns, the spectrum is already dominated by discrete zirconium neutral-atomic lines. Both Zr II line at 462.91 nm and ZrO molecular band ($\alpha(0,0)$ band of the $d^3\Delta_3 - d^3\Delta_3$ system) are weak but distinguishable. The Zr I lines are broadened by Stark effect. The plasma obviously split into two parts and the behaviors of the two parts are significantly

different. The intensity of Zr I 462.64 nm verse plasma height is shown in Fig. 6(a). The height of the plasma portion at the bottom (*Zone I*) was around 0.8 mm, and only slight increase was observed as function of delay. However, the plasma portion at the top (*Zone II*) features more distinguishable dynamics. The plasma height increased about 1.2 mm from 0.5 μs to 3 μs, but the lengths (defined as the length of single split plasma plume in vertical direction) remained similar for all detection delays.
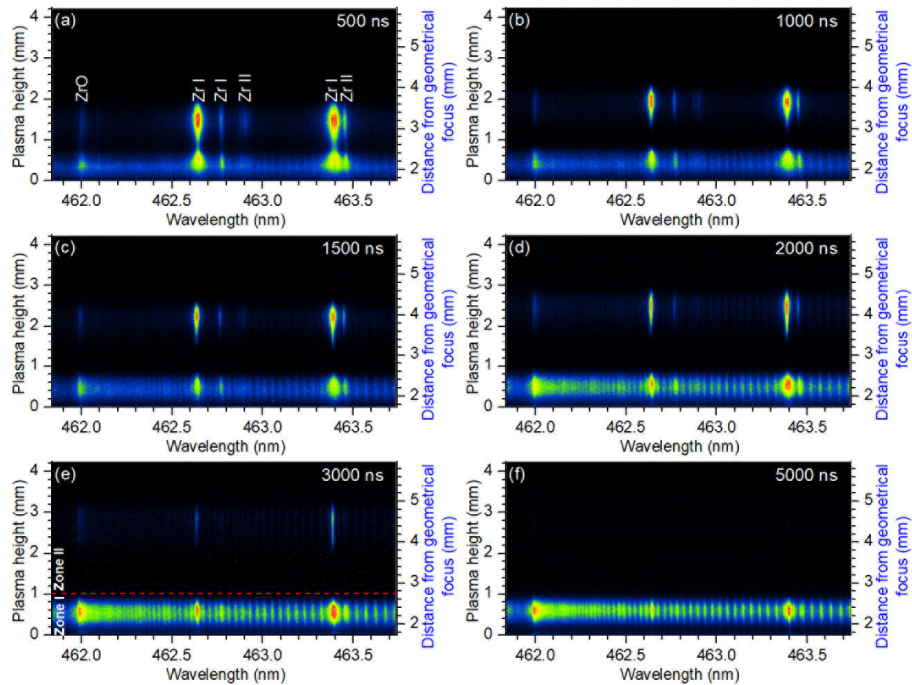

Fig. 5. Temporal and spatial resolved plasma emission spectra recorded by two dimensional ICCD array. Zirconium metal sample was placed at position of H4. *Zone I* is the bottom of plasma and *Zone II* is the top plasma, as shown in (e).
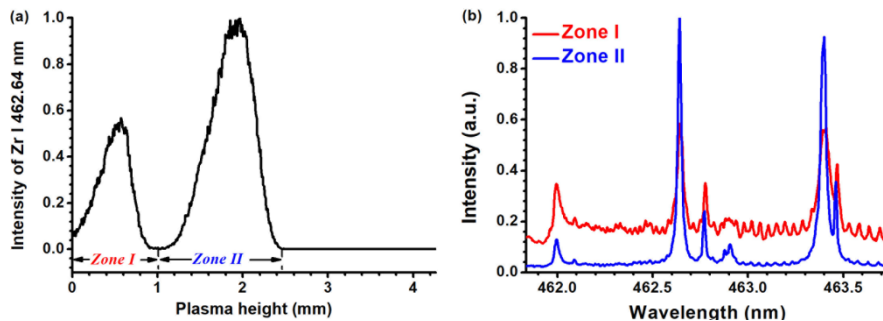

Fig. 6. (a) Intensity distribution of Zr I 462.64 nm versus plasma height. Continuum and molecular emission components were subtracted, and intensity was further normalized by dividing the maximum. (b) Spectra obtained by integrating ICCD pixel counts corresponding to *Zone I* and *Zone II*, respectively. Dark current was subtracted and the two spectra were normalized by dividing maximum intensity. The gate delay was 1000 ns and gate width was 500 ns.
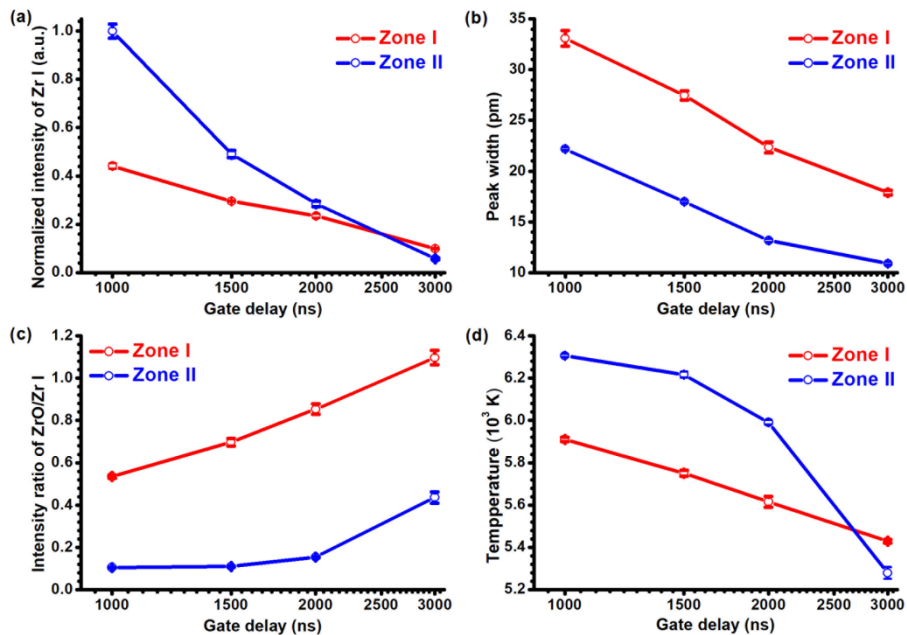
Fig. 7. Temporal evolutions of (a): intensity of Zr atomic line at 462.64 nm, (b): peak width of Zr I 462.64 nm, (c): intensity ratio of ZrO molecular bandhead to Zr I 462.64 nm, and (d): excitation temperature for two separate portions of plasma induced at position H4. For late plasma, plasma plume split into two parts, the one close to sample was defined as *Zone I* and another part was defined as *Zone II*.

In order to further characterize the spectral emission from *Zone I* and *Zone II* plasma portions, two spectra were extracted from each frame by integrating vertical pixels regions (whole zone) that corresponding to *Zone I* and *Zone II*, respectively. Two typical spectra taken at delay time of 1000 ns were shown in Fig. 6(b). The continuum component of spectrum acquired from *Zone I* is about 4.7 times of that from *Zone II*, and the intensities of atomic lines from *Zone II* are much higher than that from *Zone I*. For different delay times, the integrated pixel region for each zone was modified with respect to the intensity distribution versus plasma height, as shown in Fig. 6(a). Following a fitting procedure, component of atomic lines, ionic line and ZrO molecular bands were de-convoluted from spectra. The fitting procedure was reported in our previous work [19]. By analyzing series images acquired with different delay times, the evolution of Zr I 462.64 nm intensity, peak width of Zr I 462.64 nm, intensity ratio of ZrO bandhead to Zr I 462.64 nm were obtained, as shown in Figs. 7(a)-7(c). At initial delay time of 1 μs, the Zr I line intensity of *Zone II* is about two times than that of *Zone I*, but the intensity decays faster. For the plasma portion inside the weakly ionized channel, the recombination possibility of zirconium atoms and oxygen atoms is low because the oxygen molecules density was low inside the weakly ionized channel, and the outward shockwave propagation is likely to prohibit the chemical interaction between plasma plumes and ambient air [47]. The majority oxygen atoms that form ZrO molecules are from air oxygen molecule. In such low air molecular density environment, lower molecular emission intensity is expected, and confirmed by experimental result shown in Fig. 7(c). The intensity ratios of ZrO to Zr I from *Zone I* are about three times higher than that of *Zone II* at any gate delay. Lower collision process is also expected for plasmas formed in low density channel, which is evidenced by comparison of evolution of Zr I peak width obtained from two zones as shown in Fig. 7(b). Narrower peak width indicates lower electron density because Stark collision dominates the broadening the atomic lines in laser induced plasma [48]. The electron density of Zone *II* is estimated to be about 30%-40%

lower than that of Zone *I*. The reduced spectral line broadening favors isotope analysis with LIBS technique, because the isotope shift of atomic lines of high-Z elements (e.g. U) is very small and cannot be well resolved due to the broadening of atomic lines [49]. Plasma temperatures are also deduced utilizing Boltzmann-Plot method, as previous reported [19]. The evolutions of plasma temperature are shown in Fig. 7(d). The fast temperature decay is the key reason leads to the intensity decay of atomic lines.

4. Conclusion

In conclusion, we reported a novel method to create high temperature, low electron density plasma with intense elemental emission and weak bremsstrahlung emission. Weakly ionized air channels were generated by focusing ultrafast laser beams. Femtosecond laser ablated plasma plume can be sucked into the long-lived underdense channel that created by ultrafast laser filamentation phenomenon, and further split into two parts whilst longer weakly ionized air channel formed above the ablation spot. The two split plasma plumes were characterized by analyzing the spectral emission and the result showed that the part of plasma sucked into weakly ionized air channels features higher initial temperature, lower electron density and faster decay. The plasma portion sucked into weakly ionized plasma channels emits very clean atomic and molecular spectra, which favors chemical analysis performance improvement. Instead, distinct continuum component contributes to the spectra taken from plasma portion near sample surface. The reported arresting phenomenon will be especially useful for isotope analysis with LIBS technique using spectra from zone *II*. For Laser ablation molecular isotopic spectrometry (LAMIS) technique, spectra from Zone *I* can be used for isotope analysis since the molecular emission is more favorable at this zone. Moreover, the plasma portion at the top is almost free of bremsstrahlung emission, which is very helpful for general LIBS signal analysis because reduced collisions lead to higher resolution emission lines, and even enables detection of LIBS signal with non-gated detector.

Funding